Axial creeping flow in the gap between a rigid cylinder and a concentric elastic tube

S. B. Elbaz[1] **and A. D. Gat**[1],†

[1]Faculty of Mechanical Engineering, Technion – Israel Institute of Technology, Haifa 32000, Israel

We examine transient axial creeping flow in the annular gap between a rigid cylinder and a concentric elastic tube. The gap is initially filled with a thin fluid layer. We employ an elastic shell model and the lubrication approximation to obtain governing equations for the elastohydrodynamic interaction. At long axial length scales viscous forces are balanced by elastic tension, while at shorter length scales the viscous–elastic balance is achieved by means of an interplay between elastic bending, tension and shear stresses. Based on a viscous gravity current analogy in the tensile–viscous regime, we devise propagation laws for displacement flows which are induced by a variety of boundary conditions and examine different limits of the prewetting thickness. Next we focus on the moving elastohydrodynamic contact line at the edge of a penetrating film. A uniform matched asymptotic solution connecting the interior tension-based region with a boundary layer region near the propagation front is presented. Finally, a constructive example is shown in which isolated moving deformation patterns are created and superimposed to form a travelling wave displacement field. The presented interaction between viscosity and elasticity may be applied to fields such as soft robotics and micro-scale or larger swimmers by allowing for the time-dependent control of an axisymmetric compliant boundary.

Key words: low-Reynolds-number flows

1. Introduction

We examine the effect of elasticity on transient axial creeping flow in the annular gap between a rigid cylinder and a concentric elastic tube. The gap between the cylinder and tube is assumed small compared with the radius and length of the cylinder. The flow field is modelled by applying the lubrication approximation, while the external elastic tube is modelled by thin shell theory. We focus on viscous–elastic time scales and nonlinear dynamics, where elastic deformation significantly modifies the boundaries of the fluidic region.

A previous work (Elbaz & Gat 2014) examined viscous flow through a slender elastic cylindrical shell, subjected to an external stress field, as a simple model of a soft robot. Under an assumption of small elastic deformations, the analysis yielded a governing inhomogeneous linear diffusion equation and several solutions were

examined in the context of soft-robotic applications. Compressibility of the shell material was shown to strongly affect the flow and deformation regimes.

The annular configuration examined in the current work allows for solid deformations to be small compared with the elastic scale but significant in the fluidic domain, thus enabling the use of thin shell theory to study nonlinear viscous–elastic interaction. A similar configuration was examined by Paidoussis (1998) who focused on high Reynolds numbers. The interaction of elastic tubes and thin viscous flows, at the limit of low Reynolds numbers, has been studied by Halpern & Grotberg (1992) and White & Heil (2005) who, among others, analysed the dynamics of a liquid film coating the inner surface of an elastic tube in the context of flows in small airways in the lungs. Other studies involving a thin creeping flow between a rigid surface and an elastic surface focused on planar configurations. These include Chauhan & Radke (2002), who modelled the dynamics of a contact lens during blinking as a thin viscous film contained between an elastic shell and a flat rigid surface. Pihler-Puzović *et al.* (2012) and Al-Housseiny, Christov & Stone (2013) studied the effect of elasticity on the onset of Taylor–Saffman fingering instability in Hele-Shaw cells. Pihler-Puzović, Juel & Heil (2014) related the patterns of viscous fingering to patterns of wrinkling in an elastic Hele-Shaw cell. Trinh, Wilson & Stone (2014*a*) and Trinh, Wilson & Stone (2014*b*) studied rigid and elastic plates, either pinned or free floating, moving over a viscous film laying on a flat rigid surface. Carlson, Mandre & Mahadevan (2015) studied the deformation and flow field created by a propagating adhesion front attaching an elastic sheet to a rigid surface, where the gap between the elastic sheet and rigid surface is filled with a viscous fluid.

For the case in which there is initially a small gap between the rigid cylinder and the elastic tube, the examined problem can be viewed as a cylindrical version of the peeling problem (McEwan & Taylor 1966; Hosoi & Mahadevan 2004; Lister, Peng & Neufeld 2013). In this regard, the peeling formation of the current study bears mathematical proximity to a viscous gravity current (e.g. Buckmaster 1977; Huppert 1982; Momoniat 2006). Gravity currents have also been studied in geophysical contexts when coupled with elastic surfaces (Howell, Robinson & Stone 2013; Balmforth, Craster & Hewitt 2015; Hewitt, Balmforth & De Bruyn 2015).

The suggested configuration may have bearing on models of compliant boundaries (Gad-el Hak 2002), axisymmetric swimmers (Setter, Bucher & Haber 2012; Toppaladoddi & Balmforth 2014) and soft-robotic applications (Rus & Tolley 2015). The structure of this work is as follows: in § 2 the geometry, relevant parameters and physical assumptions are defined. In § 3 elastic shell theory and the lubrication approximation are employed to obtain governing equations for the elastohydrodynamic interaction. Section 4 presents closed-form solutions of the governing equations. The interior tensile–viscous regime is described in § 4.1, where we devise propagation laws for different types of boundary conditions and prewetting scales. The dynamics near the propagation front is described in § 4.2, where a uniform matched asymptotic solution connecting the interior region far from the front with a boundary layer region near the front is presented. Section 4.3 examines isolated moving deformations for the case of relative axial speed between the rigid cylinder and the elastic tube. Concluding remarks are presented in § 5.

2. Problem formulation

We study Newtonian, incompressible, axial creeping flow in the annular gap between a rigid cylinder and a concentric elastic tube, under the limitations of linear
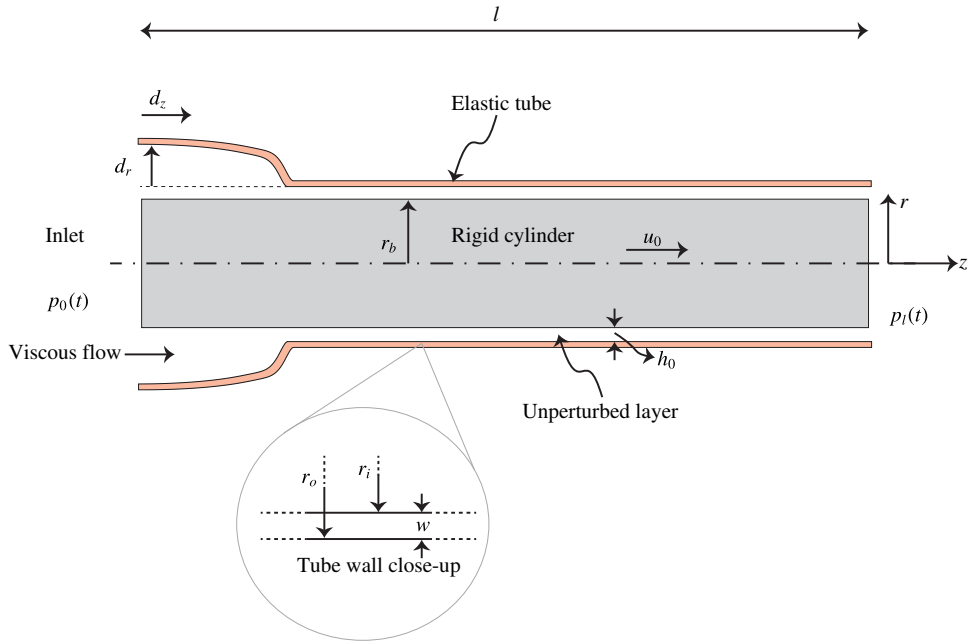
FIGURE 1. (Colour online) Schematic illustration of the elastic tube and annular fluid layer enclosing a rigid cylinder. We define the cylindrical coordinates (r, z). Radial and axial solid deformations are denoted d_r, d_z, respectively. The radius of the cylinder is r_b. The dynamic inner and outer surfaces of the elastic tube resulting from the displacement flow are $r_i + d_r(z, t)$ and $r_o + d_r(z, t)$, respectively. The wall thickness of the tube is denoted by $w = r_o - r_i$. The penetrating film also causes axial displacement of the tube: a material point z shifts to $z + d_z(z, t)$. The unperturbed (prewetting) layer is denoted h_0. The dynamic annular gap, between the cylinder and the elastic tube, is $h_0 + d_r(z, t)$. Inlet pressures denoted $p_0(t)$ (left) and $p_l(t)$ (right) are arbitrary functions of time t.

elasticity. The cylindrical coordinate system is defined in figure 1 with the axial direction along z and radial direction along r. A prewetting layer is contained in the gap between the cylinder and the tube and is assumed sufficient so that van der Waals forces can be neglected. Viscous flow due to time-varying inlet pressure as well as relative axial speed between the cylinder and tube will create both radial and axial deformation of the tube. The height of the film contained in the gap, measured radially from the cylinder to the displaced tube, is assumed small compared to the radius and length of the cylinder. We focus on viscous–elastic interaction regimes, where the elastic shell is sufficiently soft that it is deformed significantly by the fluid flow.

Hereafter, normalized variables are denoted by uppercase letters and characteristic parameters are denoted by lowercase letters with asterisks (e.g. if a is a dimensional variable, a^* is the characteristic value of a and $A = a/a^*$ is the corresponding normalized variable).

The relevant variables and parameters are time t, axial coordinate z, radial coordinate r, axial liquid speed u_z, radial liquid speed u_r, liquid pressure p, liquid viscosity μ, liquid density ρ, solid axial deformation d_z, solid radial deformation d_r, solid strain e_{ij} and stress σ_{ij} (acting on the plane normal to coordinate i and in the direction of coordinate j), tube inner radius r_i and outer radius r_o (see figure 1), tube

midsection, $r_m = (r_i + r_o)/2$, rigid cylinder radius r_b and the length l of the cylinder and tube in the z direction.

The prewetting layer is defined as the gap between the cylinder and inner tube radius, $h_0 = r_i - r_b$, when at rest. We define an auxiliary radial coordinate, $s = r - r_b$. The slenderness ratio of the cylinder and tube is defined as

$$\epsilon = \frac{r_b}{l}. \tag{2.1}$$

The ratio of prewetting thickness to characteristic radial deformation is defined by

$$\lambda_h = \frac{h_0}{d_r^*}. \tag{2.2}$$

Small parameters in the analysis include the ratio between the characteristic radial deformation d_r^* and the length of the cylinder and tube in the z direction,

$$\frac{d_r^*}{l} = \varepsilon_1 \ll 1, \tag{2.3}$$

ratio of wall thickness $w = r_o - r_i$ to inner tube radius r_i,

$$\frac{w}{r_i} = \varepsilon_2 \ll 1 \tag{2.4}$$

and small elastic deformations, expressed by the ratios,

$$\frac{d_r^*}{r_i} \sim \frac{d_z^*}{l} = \varepsilon_3 \ll 1, \tag{2.5}$$

where d_z^* is the corresponding characteristic axial deformation. We assume negligible inertia,

$$\frac{d_r^*}{l} \frac{\rho u_z^* d_r^*}{\mu} \ll 1, \tag{2.6}$$

where u_z^* is characteristic axial liquid velocity (a detailed discussion of the condition of negligible inertia is presented in § 3.3).

3. Analysis

In order to obtain governing equations for the elastohydrodynamic interaction, we apply the lubrication approximation for the flow field and the Kirchhoff–Love thin shell approximation for the solid deformation field, under the requirement of similar time scales of both elastic and fluidic dynamics.

3.1. *The elastic problem*

The deformation field of axisymmetric linearly elastic material with negligible inertia is governed by the momentum equations,

$$\frac{\partial}{\partial r}(r\sigma_{rr}) + \frac{\partial}{\partial z}(r\sigma_{zr}) - \sigma_{\theta\theta} = 0, \quad \frac{\partial}{\partial r}(r\sigma_{zr}) + \frac{\partial}{\partial z}(r\sigma_{zz}) = 0, \tag{3.1a,b}$$

the strain–displacement relations,

$$e_{rr} = \frac{\partial d_r}{\partial r}, \quad e_{\theta\theta} = \frac{d_r}{r}, \quad e_{zz} = \frac{\partial d_z}{\partial z}, \quad e_{zr} = \frac{1}{2}\left(\frac{\partial d_r}{\partial z} + \frac{\partial d_z}{\partial r}\right), \quad (3.2a\text{--}d)$$

and Hooke's law,

$$Ee_{zr} = (1+\nu)\sigma_{zr}, \quad Ee_{rr} = \sigma_{rr} - \nu(\sigma_{zz}+\sigma_{\theta\theta}), \quad Ee_{\theta\theta} = \sigma_{\theta\theta} - \nu(\sigma_{rr}+\sigma_{zz}), \quad (3.3a\text{--}c)$$

$$Ee_{zz} = \sigma_{zz} - \nu(\sigma_{rr}+\sigma_{\theta\theta}), \quad (3.3d)$$

where E is Young's modulus and ν is Poisson's ratio. The boundary conditions for the stress applied by the liquid at $r = r_i + d_r$ are

$$\sigma_{rr}(r = r_i + d_r) = -p + 2\mu\frac{\partial u_r}{\partial r}, \quad \sigma_{zr}(r = r_i + d_r) = \mu\left(\frac{\partial u_z}{\partial r} + \frac{\partial u_r}{\partial z}\right), \quad (3.4a,b)$$

and at $r = r_o + d_r$ the stress vanishes

$$\sigma_{rr}(r = r_o + d_r) = 0, \quad \sigma_{zr}(r = r_o + d_r) = 0. \quad (3.4c,d)$$

We define normalized coordinates, $(R, Z) = (r/r_b, z/l)$, normalized radial and axial deflections, $(D_r, D_z) = (d_r/d_r^*, d_z/d_z^*)$ and normalized liquid pressure, $P = p/p^*$, where p^* is the characteristic pressure representing the order of magnitude of the inlet pressure. As we shall see it is related to the characteristic radial deformation by $p^* = d_r^* E \varepsilon_2 / r_b$. However, the configuration may also be actuated by forced initial deformation of the shell, in which case d_r^* should be chosen to represent the characteristic initial deformation and p^* is then obtained by the appropriate relation. Following elastic shell theory (Mollmann 1981), we define stress resultants for the forces n_{ij} and moments m_{ij} as

$$n_{ij} = \int_{r_i}^{r_o} \sigma_{ij}\,\mathrm{d}r, \quad m_{ij} = \int_{r_i}^{r_o} \sigma_{ij} r\,\mathrm{d}r. \quad (3.5a,b)$$

We first integrate the axial momentum equation with respect to r, from r_i to r_o, to obtain an axial force balance,

$$\sigma_{zr}(r_i) \sim \frac{\partial n_{zz}}{\partial z}. \quad (3.6)$$

We now multiply the axial momentum equation by $r - r_m$ and integrate once more over r to obtain a resultant form. We then differentiate with respect to z in order to relate to the radial momentum equation (3.1). This yields

$$\frac{\partial n_{zr}}{\partial z} \sim \frac{\partial^2 m_{zz}}{\partial z^2} + \left(\frac{\varepsilon_2 r_m}{2} - r_i\right)\frac{\partial \sigma_{zr}(r_i)}{\partial z}, \quad (3.7)$$

where we've also substituted (3.6).

Substituting into the resultant form of the radial momentum equation,

$$n_{\theta\theta} \sim r_i p + r_i\left(\frac{\partial^2 m_{zz}}{\partial z^2} + \left(\frac{\varepsilon_2 r_m}{2} - r_i\right)\frac{\partial \sigma_{zr}(r_i)}{\partial z}\right). \quad (3.8)$$

The normal and shear stress scale as $\sigma_{rr} \sim p$ and $\sigma_{zr} \sim \varepsilon_1 p$ (this is obtained from the fluidic problem, see §3.2). Order of magnitude analysis of (3.6) yields the following scaling relations,

$$n_{zz} \sim d_r p, \quad \sigma_{zz} \sim \frac{p}{\varepsilon_2} \varepsilon_3, \tag{3.9a,b}$$

and order of magnitude analysis of (3.8) yields

$$n_{\theta\theta} \sim r_b p, \quad \sigma_{\theta\theta} \sim \frac{p}{\varepsilon_2}. \tag{3.10a,b}$$

Taking note that $m_{zz} \sim r_b n_{zz}$, normalizing (3.8) yields,

$$N_{\theta\theta} \sim P + \varepsilon_1 \epsilon \left[\frac{\partial^2 M_{zz}}{\partial Z^2} + (\varepsilon_2 - 1) \frac{\partial \Sigma_{zr}(1, Z)}{\partial Z} \right], \tag{3.11}$$

where we've retained the higher derivative of the bending moment M_{zz} and the shear stress at the fluid interface $\partial \Sigma_{zr}(1, Z)/\partial Z$. We normalize Hooke's law (3.3) according to the above characteristic values and attain a reduced form of Love's first approximation (Love 1888),

$$\varepsilon_3 \Sigma_{zz} \sim \frac{\varepsilon_2 E}{p^*(1 - \nu^2)} (e_{zz} + \nu e_{\theta\theta}) \tag{3.12}$$

$$\Sigma_{\theta\theta} \sim \frac{\varepsilon_2 E}{p^*(1 - \nu^2)} (e_{\theta\theta} + \nu e_{zz}). \tag{3.13}$$

We apply (Dugdale & Ruiz 1971) the Kirchhoff hypothesis and describe the displacement field in terms of the radial $\bar{d}_r$ and axial $\bar{d}_z$ displacements of the midsection, denoted by overbars,

$$\bar{d}_z = d_z + (r - r_m) \frac{\partial d_r}{\partial z}, \quad \bar{d}_r = d_r, \tag{3.14a,b}$$

and thus we can represent the strain as a function of the deformation by

$$e_{zz} = \frac{\partial \bar{d}_z}{\partial z} - (r - r_m) \frac{\partial^2 \bar{d}_r}{\partial z^2}, \quad e_{\theta\theta} = \frac{\bar{d}_r}{r}. \tag{3.15a,b}$$

Integrating (3.12), (3.13) over r into resultant form and evaluating the moment M_{zz}, we find that

$$N_{zz} \sim \frac{E\varepsilon_2}{p^*(1 - \nu^2)} \left(\frac{\partial \bar{D}_z}{\partial Z} + \nu \bar{D}_r \right), \tag{3.16}$$

$$N_{\theta\theta} \sim \frac{E\varepsilon_2 \varepsilon_3}{p^*(1 - \nu^2)} \left(\nu \frac{\partial \bar{D}_z}{\partial Z} + \bar{D}_r \right), \tag{3.17}$$

and

$$M_{zz} \sim \frac{E\varepsilon_2}{p^*(1 - \nu^2)} \left[\frac{\partial \bar{D}_z}{\partial Z} - \frac{\epsilon^2 \varepsilon_2^2}{12} \frac{\partial^2 \bar{D}_r}{\partial Z^2} + \nu \bar{D}_r \right], \tag{3.18}$$

where $\bar{D}_r$, $\bar{D}_z$ are the non-dimensional displacements of the midsection. The term $\partial \bar{D}_z/\partial Z$ can be evaluated between (3.6) and (3.16). We can now express (3.11) in terms of fluid pressure and radial deformation,

$$\frac{\epsilon^4 \varepsilon_2^2}{12(1-\nu^2)} \frac{\partial^4 \bar{D}_r}{\partial Z^4} - \frac{\epsilon \varepsilon_1 \varepsilon_2}{2} \frac{\partial \Sigma_{zr}(1,Z)}{\partial Z} + \bar{D}_r \sim P. \quad (3.19)$$

The leading order of (3.19) is a tensile regime in which $\bar{D}_r \sim P$. However, the small term $(\epsilon^4 \varepsilon_2^2/12(1-\nu^2))\partial^4 \bar{D}_r/\partial Z^4$ may become dominant in a boundary layer near the location of a fixed end of the tube or near a peeling front, as the fluid layer thickness goes to zero at the edge of a penetrating film. The small term $(\epsilon \varepsilon_1 \varepsilon_2/2)\partial \Sigma_{zr}(1,Z)/\partial Z$, as we shall see, increases inversely with the fluid layer thickness near the peeling front and thus will undergo rescaling in the contact line analysis (see §4.2).

The corresponding relation between radial and axial deformations reads

$$\bar{D}_z(Z,T) - \bar{D}_z(Z=0,T) \sim -\nu \int_0^Z \bar{D}_r(\zeta,T)\,\mathrm{d}\zeta, \quad (3.20)$$

which simply describes the stretching of the tube as it expands; a result of Poisson's effect. We conclude the elastic analysis with the relation between the characteristic radial deformation and characteristic pressure, representing the dominant elastic tension to viscous force balance,

$$\frac{p^*}{E\varepsilon_2} = \frac{d_r^*}{r_b} = \varepsilon_3 \ll 1. \quad (3.21)$$

Equation (3.21) provides limitation on the maximal allowed pressure for which the assumption of small deformations is valid. Hereafter the midsection overbars are omitted for simplicity.

3.2. *The fluidic problem*

We assume an axisymmetric incompressible Newtonian flow, governed by the momentum equations,

$$\rho\left(\frac{\partial u_r}{\partial t} + u_r\frac{\partial u_r}{\partial r} + u_z\frac{\partial u_r}{\partial z}\right) = -\frac{\partial p}{\partial r} + \mu\left[\frac{1}{r}\frac{\partial}{\partial r}\left(r\frac{\partial u_r}{\partial r}\right) + \frac{\partial^2 u_r}{\partial z^2} - \frac{u_r}{r^2}\right], \quad (3.22)$$

$$\rho\left(\frac{\partial u_z}{\partial t} + u_r\frac{\partial u_z}{\partial r} + u_z\frac{\partial u_z}{\partial z}\right) = -\frac{\partial p}{\partial z} + \mu\left[\frac{1}{r}\frac{\partial}{\partial r}\left(r\frac{\partial u_z}{\partial r}\right) + \frac{\partial^2 u_z}{\partial z^2}\right] + \rho g, \quad (3.23)$$

and conservation of mass,

$$\frac{1}{r}\frac{\partial}{\partial r}(ru_r) + \frac{\partial u_z}{\partial z} = 0. \quad (3.24)$$

The relevant boundary conditions are no slip and no penetration at $r = r_i + d_r$,

$$u_r(r = r_b + h_0 + d_r) = \frac{\partial d_r}{\partial t}, \quad u_z(r = r_b + h_0 + d_r) = \frac{\partial d_z}{\partial t}, \quad (3.25a,b)$$

and at the rigid cylinder boundary, $r = r_b$,

$$u_r(r = r_b) = 0, \quad u_z(r = r_b) = u_0. \quad (3.26a,b)$$

Pressure at the inlet and outlet may be governed by

$$p(z = 0) = p_0(t), \quad p(z = l) = p_l(t), \tag{3.27a,b}$$

where $p_0(t)$ and $p_l(t)$ are arbitrary functions of time having order of magnitude p^*. We define normalized liquid velocities $(U_r, U_z) = (u_r/u_r^*, u_z/u_z^*)$, and normalize the coordinate $s = r - r_b$, defined in the gap $0 \leqslant s \leqslant h_0 + d_r(z, t)$, by d_r^*,

$$S = \frac{s}{d_r^*}, \quad 0 \leqslant S \leqslant \lambda_h + D_r(Z, T). \tag{3.28}$$

Order of magnitude analysis of (3.24) yields

$$\frac{u_r^*}{u_z^*} \sim \frac{d_r^*}{l} = \varepsilon_1, \quad u_z^* = \frac{\varepsilon_1 d_r^* p^*}{\mu}. \tag{3.29}$$

We require $u_0 \sim u_z^*$ so that the viscous stresses resulting from the motion of the rigid cylinder scale as $\mu u_0/d_r^*$. We focus on negligible gravity, $G = \rho g l/p^* \ll 1$, and define the Reynolds number, $Re = \rho u_z^* d_r^*/\mu$ and the Womersley number, $W^2 = \rho d_r^{*2}/\mu t^*$. We transform (3.22)–(3.24) from $R \rightarrow S$ and employ (3.29). The result is the following reduced system for the fluidic domain,

$$\frac{\partial P}{\partial Z} = \frac{\partial^2 U_z}{\partial S^2} + O(W^2, \varepsilon_3, \varepsilon_1 Re, \varepsilon_1^2, G), \tag{3.30a}$$

$$\frac{\partial P}{\partial S} = O(W^2, \varepsilon_1^3 Re, \varepsilon_1^2), \tag{3.30b}$$

$$\frac{\partial U_r}{\partial S} + \frac{\partial U_z}{\partial Z} = O(\varepsilon_3). \tag{3.30c}$$

The boundary conditions (3.25), (3.26) take the normalized form,

$$U_r(S = \lambda_h + D_r) = \frac{\partial D_r}{\partial T}, \quad U_z(S = \lambda_h + D_r) = \frac{d_z^*}{t^* u_z^*} \frac{\partial D_z}{\partial T}, \tag{3.31a,b}$$

and

$$U_r(S = 0) = 0, \quad U_z(S = 0) = U_0, \tag{3.31c,d}$$

with $U_0 = u_0/u_z^*$ and $T = t/t^*$, where $t^* \sim d_r^*/u_r^*$ is the time scale of the viscous–elastic interaction to be defined shortly (see (3.35)). We solve (3.30a), (3.30b) imposing conditions (3.31). The resulting leading-order axial speed U_z reads

$$U_z \sim \frac{1}{2} \frac{\partial P}{\partial Z}[S^2 - (\lambda_h + D_r)S] + \frac{S}{(\lambda_h + D_r)} \frac{d_z^*}{t^* u_z^*} \frac{\partial D_z}{\partial T} + U_0 \left[1 - \frac{S}{(\lambda_h + D_r)}\right], \quad (3.32)$$

and is defined for $\lambda_h + D_r \geqslant 0$. Addressing mass conservation (3.30c), we install (3.32) and integrate with respect to S across the film layer to produce a reduced Reynolds equation relating fluidic pressure to elastic deformations,

$$\frac{\partial D_r}{\partial T} - 4 \frac{\partial}{\partial Z} \left\{ \frac{\partial P}{\partial Z}(\lambda_h + D_r)^3 \right\} + 24 U_0 \frac{\partial D_r}{\partial Z}$$

$$\sim \frac{\varepsilon_3}{2} \left[\frac{\partial D_r}{\partial Z} \frac{\partial D_z}{\partial T} - (\lambda_h + D_r) \frac{\partial^2 D_z}{\partial Z \partial T} \right]. \tag{3.33}$$

Equation (3.33) is valid for $\lambda_h + D_r \geqslant 0$. The residual axial speed correction terms (of order $O(\varepsilon_3)$) have been included for reference.

3.3. *The fluidic–elastic problem*

Equations (3.19) and (3.33) yield a coupled set in pressure and deformation which governs the elastohydrodynamic interaction (for the corresponding dimensional equations see (A 1)),

$$\frac{\epsilon^4 \varepsilon_2^2}{12(1-\nu^2)} \frac{\partial^4 D_r}{\partial Z^4} - \frac{\epsilon \varepsilon_1 \varepsilon_2}{2} \left[\frac{(\lambda_h + D_r)}{2} \frac{\partial^2 P}{\partial Z^2} + \left(\frac{U_0}{(\lambda_h + D_r)^2} - \frac{1}{2} \frac{\partial P}{\partial Z} \right) \frac{\partial D_r}{\partial Z} \right] + D_r \sim P,$$

(3.34a)

$$\frac{\partial D_r}{\partial T} \sim 4 \frac{\partial}{\partial Z} \left\{ \frac{\partial P}{\partial Z} (\lambda_h + D_r)^3 \right\} - 24 U_0 \frac{\partial D_r}{\partial Z}.$$

(3.34b)

The shear term of (3.19) was evaluated via the lubrication approximation (3.30). Equation (3.34a) implies an outer regime in which bending and shear stresses can be neglected and a balance between elastic tension and viscous forces dominates. Near boundaries such as a fixed connection to a rigid wall or near the moving peeling front, elastic bending may become part of the dominant balance inside a boundary layer region. The middle term of (3.34b) represents the effect of competing elastic forces on the pressure driven Poiseuille flow of the film. The motion of the rigid cylinder also drives a Couette flow which transports deformations along the axis (right-hand term of (3.34b)). The characteristic time scale t^* is evaluated via relations (3.21) and (3.29) (an extra factor of 48 is included for convenience),

$$t^* = \frac{48(E\varepsilon_2)^2 \mu}{p^{*3} \epsilon^2} = \frac{48(Ew)^2 l^2 \mu}{p^{*3} r_b^4},$$

(3.35)

and is written in terms of the characteristic driving pressure. This dependence stems from the nonlinearity of (3.34b). Equation (3.35) enables us to estimate an upper limit on the characteristic pressure beyond which the assumption of negligible inertia (3.30a)–(3.30b) will no longer be valid, representing the range of validity of the analysis. Substituting (3.35) into (3.30a), we demand that both W^2 and $\varepsilon_1 Re$ terms be negligible and derive the condition that

$$p^* \ll \left(\frac{\mu}{\epsilon r_b} \right)^{2/5} \frac{(E\varepsilon_2)^{4/5}}{\rho^{1/5}} = \frac{(\mu l)^{2/5} (Ew)^{4/5}}{r_b^{8/5} \rho^{1/5}}.$$

(3.36)

We note that for the case of small deformations compared with the prewetting thickness ($d_r \ll h_0$), bending and shear stresses can be neglected, and hence (3.34a) reduces to $D_r \sim P$. Substituting back into (3.34b) and setting $D_r \ll \lambda_h$ in the diffusion coefficient yields the linearized form

$$\frac{\partial D_r}{\partial T} \sim 4 \frac{\partial^2 D_r}{\partial Z^2},$$

(3.37)

where the transport effect of the rigid cylinder motion vanishes at the presence of a thick intermediate layer. For the linear case, the appropriate time scale instead of t^* is $r_b^2 l^2 \mu / Ew h_0^3$ and shows exclusive dependence in solid–liquid material properties and the geometry of the configuration. A result which is consistent with the linear interaction time scale of the full cross-section cylindrical shell (Elbaz & Gat 2014).

4. Results

4.1. *The tensile–viscous regime*

In the following analysis we shall assume that the viscous dissipation near the apparent contact line is negligible compared with the viscous dissipation in the bulk of the fluid. Consequently, we shall first seek a solution in the form of an interior profile, balancing elastic tension and viscous forces in (3.34) under an assumption of a small, lower bounded, λ_h. In §4.2 we rescale the governing equations and examine the behaviour near the contact line, assuming conditions in the interior remain unchanged. We in turn discuss several lower bounds on λ_h which emanate from the analysis at the front.

4.1.1. *Deformation significantly larger than prewetting*

For axial length scales of $Z = O(1)$ bending and shear stresses can be neglected and hence (3.34a) reduces to $D_r \sim P$. At the limit of large deflection compared with prewetting, $\lambda_h \ll 1$ (for stationary rigid cylinder $U_0 = 0$), (3.34b) then reduces to the well-known porous medium equation (PME) in fourth power,

$$\frac{\partial D_r}{\partial T} \sim \frac{\partial^2 D_r^4}{\partial Z^2}. \tag{4.1}$$

We transform to self-similar variables,

$$D_r = T^{-\alpha} f(\eta), \quad \eta = Z T^{(3\alpha-1)/2}, \tag{4.2}$$

and follow Huppert (1982) in light of the close analogy to a viscous gravity current propagating under a density gradient.

$$F(\xi) = \eta_F^{-2/3} f(\eta), \quad \eta = \eta_F \xi. \tag{4.3}$$

Here η_F describes a propagating peeling front for which the solution is supported in the region $Z < Z_F(T)$, prior to boundary interaction $Z_F(T) < 1$. We install (4.2), (4.3) into (4.1) which then reduces to the following ordinary differential equation (ODE) in F,

$$F^{4\prime\prime} \sim \left(\frac{3\alpha - 1}{2} \right) \xi F' - \alpha F. \tag{4.4}$$

The eigenvalue α describes the height of the film at the inlet,

$$D_r(0, T) = T^{-\alpha}, \tag{4.5}$$

which equivalently represents inlet pressure in this regime. Boundary conditions are restated in F,

$$F(0) = \eta_F^{-2/3}, \quad F(\xi \geqslant 1) = 0. \tag{4.6a,b}$$

We complete the formulation with integral mass conservation represented in non-dimensional form by

$$\int_0^{Z_F(T)} D_r(Z, T) \, \mathrm{d}Z = Q T^{(1-5\alpha)/2}, \quad Q = \eta_F^{5/3} \int_0^1 F(\xi) \, \mathrm{d}\xi. \tag{4.7}$$

Both η_F and Q are functions of the eigenvalue α. Contrary to a viscous gravity current where the interface is induced by a given flux input, in which case the flux rate Q may be set constant for all α, in the current study the flux rate derives from the inlet conditions.

We first consider the specific case $\alpha = 1/5$ for which equation (4.4) may be solved analytically. The solution is a particular case of the source solution of the PME, known as the ZKB solution as it was first obtained by Zel'dovich & Kompaneets (1950) and Barenblatt (1952). The underlying boundary and initial conditions are

$$D_r(Z, 0) = Q\delta(Z), \quad \frac{\partial D_r(0, T)}{\partial Z} = 0, \tag{4.8a,b}$$

representing a sudden input of mass, Q, into the interface at $T = 0$, after which the inlet is sealed. The amplitude decay at the inlet, as the front spreads through the interface, is then given by (4.5). The solution reads

$$D_r(Z, T) = T^{-1/5}\left[1 - \frac{3}{40}Z^2 T^{-2/5}\right]_+^{1/3}, \quad Q = \frac{\sqrt{\frac{10\pi}{3}}\,\Gamma\left(\frac{4}{3}\right)}{\Gamma\left(\frac{11}{6}\right)}, \quad \eta_F = \sqrt{\frac{40}{3}}, \tag{4.9a--c}$$

where $(s)_+ = \max(s, 0)$ and Γ is Euler's gamma function. The velocity field corresponding to (4.9) can be attained via (3.32) and (3.30c). The dimensional solution corresponding to (4.9) is given by (A 2). For all other physical values of α ($\alpha < 1/5$) (4.4), along with conditions (4.6) and (4.7), must be solved numerically. In the range $\alpha \leqslant 0$ the underlying initial condition is $D_r(Z, 0) = 0$. Figure 2(a) presents the self-similar displacement profiles $F(\xi)$, analogous to a two-dimensional viscous gravity current. Figure 2(b) depicts the flux rate Q, the front locus η_F and the time it takes the front to reach the opposite boundary, denoted T_b, as a function of α. The time T_b represents the limit of validity of the self-similar analysis when adapted to a finite domain. Figure 2(c,d) depict the resulting deformation regime, D_z and D_r, respectively, for the case of constant inlet height ($\alpha = 0$). The peeling front enters from the left ($Z = 0$) while the tube is set stationary at the right end $D_r(1, T) = D_z(1, T) = 0$. The axial deformation is attained via (3.20). As the front propagates the interface, the free left end of the tube retracts towards the right; during this process we assume the inlet remains sealed.

The propagation laws for an inlet signal of type (4.5), according to self-similarity, are written in terms of the front location Z_F, accumulated mass in the interface M and time to boundary T_b,

$$Z_F = \eta_F(\alpha)T^{(1-3\alpha)/2}, \quad M = Q(\alpha)T^{(1-5\alpha)/2}, \quad T_b = \eta_F(\alpha)^{-2/(1-3\alpha)}. \tag{4.10a--c}$$

The corresponding dimensional propagation laws are given in (A 3). Relations (4.10) illustrate the dependence of the spread rate in the inlet conditions for large displacements compared with the prewetting thickness $d_r \gg h_0$. This is not the case for small displacements $d_r \ll h_0$, governed by (3.37), for which the spread rate $O(t^{1/2})$ (heat equation) is constant for all inlet conditions.
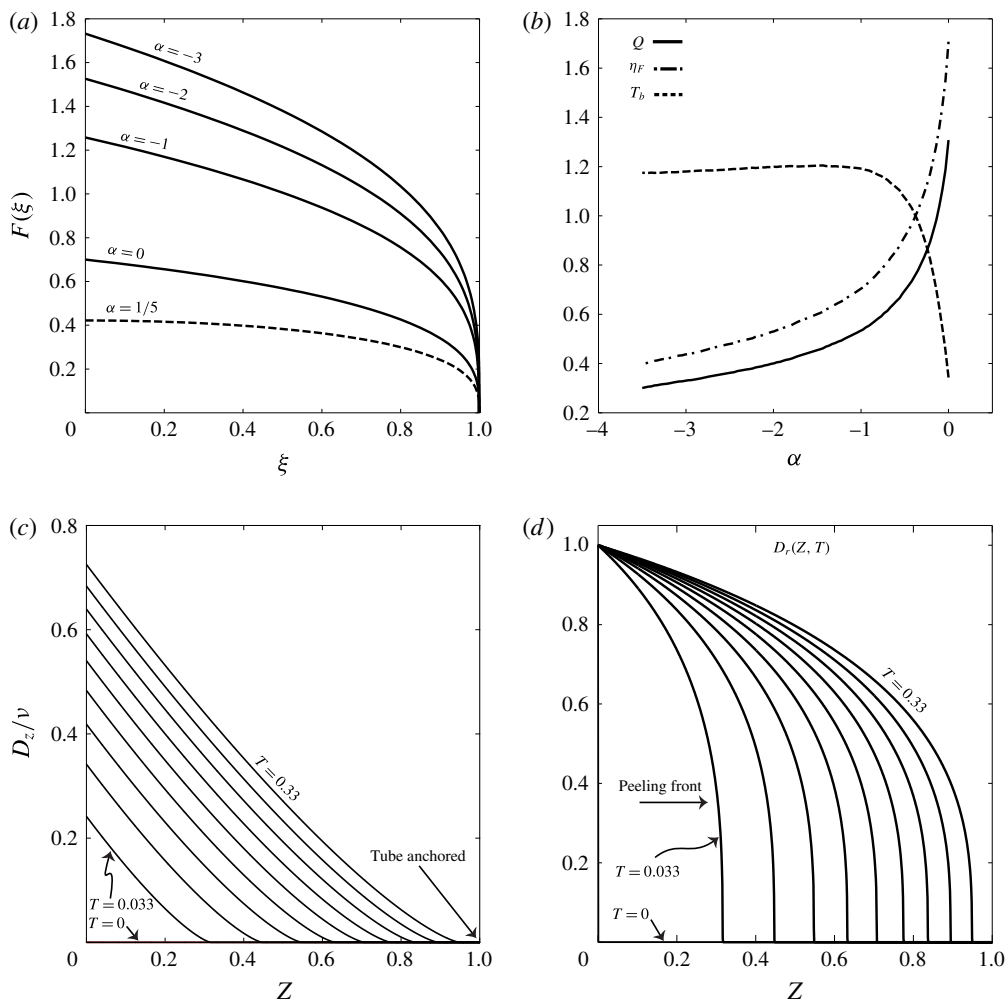
FIGURE 2. Self-similar solutions of the tensile–viscous regime, corresponding to $\lambda_h \ll 1$, $U_0 = 0$ and inlet conditions $D_r(0, T) = T^{-\alpha}$. (a) Displacement profile $F(\xi)$ corresponding to eigenvalues: $\alpha = 1/5$ (analytic – solution (4.9)) – dashed line, $\alpha = 0, -1, -2, -3$ – solid lines (obtained numerically). (b) Flux rate $Q(\alpha)$ – solid line, front locus $\eta_F(\alpha)$ – dashed-dotted line, time to boundary $T_b(\alpha) = t_b/t^*$ – dashed line (Q, η_F and T_b obtained numerically). Panel (b) is plotted in the range $\alpha \leqslant 0$ (the range $0 < \alpha \leqslant 1/5$ is irrelevant for comparison due to the change in boundary and initial conditions). (c,d) Constant-inlet-height ($\alpha = 0$) propagation in time with $\Delta T = 1/30$, between $0 \leqslant T \leqslant 1/3$, tube clamped at $Z = 1$, $D_r(1, T) = D_z(1, T) = 0$. (c) Axial deformation $D_z(Z, T)/v$. (d) Radial deformation $D_r(Z, T)$.

4.1.2. *Deformation comparable to prewetting*

When the deformation is of similar magnitude as the prewetting layer, we cannot neglect λ_h as in (4.1), but must consider the more general case,

$$\frac{\partial D_r}{\partial T} \sim 4\frac{\partial}{\partial Z}\left\{ \frac{\partial D_r}{\partial Z}(\lambda_h + D_r)^3 \right\}. \tag{4.11}$$

We note that propagation over a non-negligible prewetting layer in the current configuration is analogous to the propagation of a viscous gravity current at a fluid interface (Lister & Kerr 1989). We transform back to PME form in film height $H = \lambda_h + D_r$,

$$\frac{\partial H}{\partial T} \sim \frac{\partial^2 H^4}{\partial Z^2}, \tag{4.12}$$

and note that similarity solutions exist only for the case where there is a fixed height scale in addition to the prewetting thickness. We thus consider the case of constant-inlet-height propagation, analogous to $\alpha = 0$ in (4.5) but for general λ_h,

$$H(0, T) = 1 + \lambda_h, \quad H(Z, 0) = \lambda_h. \tag{4.13a,b}$$

We substitute $H = \tilde{f}(\eta)$, $\eta = ZT^{-1/2}$ and derive the following boundary value problem in $\tilde{f}$ (analogous to (4.4)–(4.7)),

$$\tilde{f}^{4\prime\prime} \sim -\tfrac{1}{2}\eta\tilde{f}', \tag{4.14a}$$

$$\tilde{f}(0) = 1 + \lambda_h, \quad \tilde{f}(\infty) = \lambda_h, \tag{4.14b,c}$$

$$\int_0^\infty D_r(Z, T)\, \mathrm{d}Z = \widetilde{Q}T^{1/2}, \quad \widetilde{Q} = \int_0^\infty [\tilde{f}(\eta) - \lambda_h]\, \mathrm{d}\eta. \tag{4.14d}$$

We have used the tilde symbol to denote λ_h dependency. The numerical solution of (4.14) is presented in figure 3(a) and starts from the inner profile of $D_r(\eta)$ previously attained for $\lambda_h \ll 1$. Subsequent profiles correspond to $0.1 \leqslant \lambda_h \leqslant 1$ in 0.1 increments. The resulting axial deformation profile $D_z(\eta)/\nu$ for $T = 1$, in the case where the tube is clamped ahead of any displacement, is plotted in figure 3(b); its intersection with the axis $\eta = 0$ yields the flux rate, $\widetilde{Q}(\lambda_h)$.

For non-negligible λ_h (4.11) is no longer parabolic degenerate for $D_r = 0$, causing the edge to trail to infinity. The fluid displacement travels as $O(T^{1/2})$ but is no longer compactly supported. The accumulated mass in the interface excluding the base layer is given by $\widetilde{M} = \widetilde{Q}(\lambda_h)T^{1/2}$. We would like to emphasize that this unified self-similar law of $O(t^{1/2})$ for all prewetting thicknesses is a unique property of fixed-inlet-height propagation. Note, for example, that source-type boundary conditions transition from $O(t^{1/5})$ propagation for $\lambda_h \ll 1$ (solution (4.9)) to $O(t^{1/2})$ for $\lambda_h \to \infty$ (solution of (3.37)). For intermediate values of λ_h a numerical solution is required and is illustrated below. We solve (4.11) along with appropriate boundary conditions,

$$D_r(Z, 0) = \delta(Z), \quad \frac{\partial D_r(0, T)}{\partial Z} = \frac{\partial D_r(1, T)}{\partial Z} = 0. \tag{4.15a,b}$$

A no-flux condition at the right boundary has been added to demonstrate the interaction of the front with the opposing wall. Propagation in time is shown in 3 snapshots in figure 4(a,b,c) corresponding to $T = 0.012, 0.12, 0.6$, respectively, and for varying base layer thickness $0 \leqslant \lambda_h \leqslant 3/2$. The solution was obtained via a finite difference scheme and was validated on the basis of (4.9). A faster advancement of the front as well as its spreading are observed for thicker base layers. For $\lambda_h > 1$ the solution is presented in the nonlinear time scale normalization (3.35) for comparison and converges rapidly to the behaviour of (3.37).
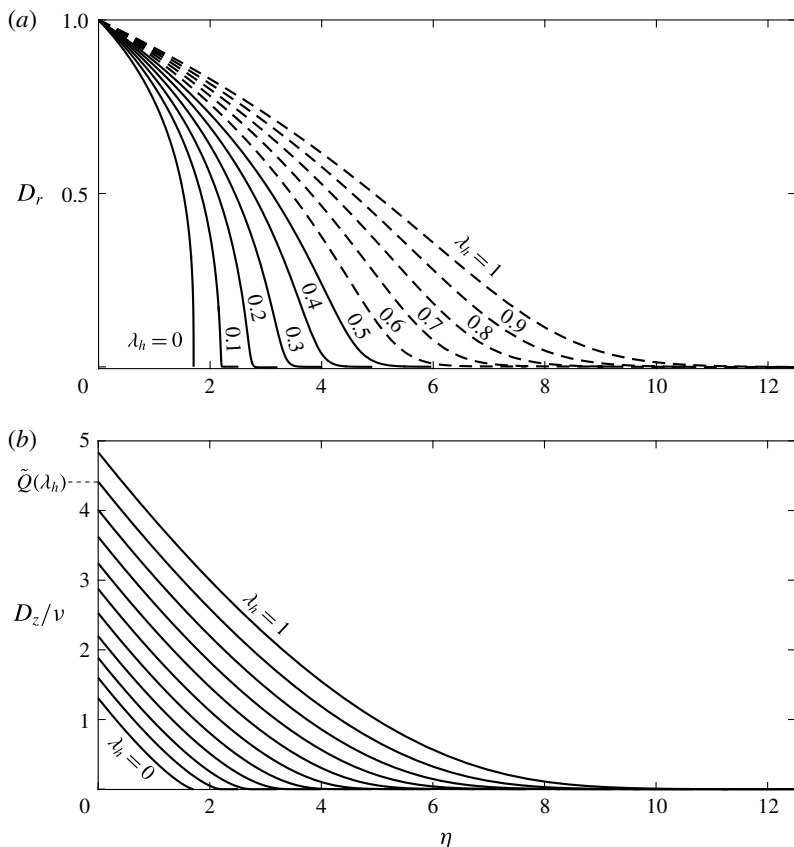
FIGURE 3. Self-similar solutions of the tensile–viscous regime for non-negligible prewetting, corresponding to $0 \leqslant \lambda_h \leqslant 1$, $U_0 = 0$ and constant inlet displacement/pressure $D_r(0, T) = 1$. (a) Radial deformation profile $D_r(\eta)$ in $\Delta\lambda_h = 0.1$ increments (obtained numerically) $0 \leqslant \lambda_h \leqslant 0.5$ – solid lines, $0.6 \leqslant \lambda_h \leqslant 1$ – dashed lines. (b) Axial deformation profile $D_z(\eta)/\nu$ at $T = 1$ in $\Delta\lambda_h = 0.1$ increments; yields the flux rate $\widetilde{Q}(\lambda_h)$ at $\eta = 0$ (tube clamped ahead of any displacement: $D_z = 0$ at $\eta \to \infty$).

4.2. *The elastohydrodynamic front*

While solution (4.9) describes a moving contact line, it neglects higher-order terms which may be dominant in its vicinity. In the following analysis we examine the viscous–elastic dynamics near the propagation front. We assume a small, lower bounded, prewetting layer $\lambda_h \ll 1$ and a shortening of the axial length scale to $Z = O(\delta)$ near the contact line. We transform (3.34) ($U_0 = 0$) to the self-similar variable $\xi = Z/Z_F$, and rescale to the boundary layer coordinate $\xi = 1 - \zeta\delta$. Equations (3.34) can be uncoupled and the result is the following ODE in the boundary layer variable $\hat{D}_r(\zeta)$, written prior to balance,

$$\frac{\epsilon^4 \varepsilon_2^2}{12(1-\nu^2) Z_F^4} \frac{1}{\delta^4} \frac{\partial^4 \hat{D}_r}{\partial \zeta^4} + \hat{D}_r \sim \delta \int_0^\zeta \frac{Z_F \dot{Z}_F \hat{D}_r(\tilde{\zeta})}{4(\lambda_h + \hat{D}_r(\tilde{\zeta}))^3} \, \mathrm{d}\tilde{\zeta} + \frac{\epsilon \varepsilon_1 \varepsilon_2}{16\delta} \frac{\dot{Z}_F}{Z_F} \frac{\lambda_h - 3\hat{D}_r}{(\lambda_h + \hat{D}_r)^3} \frac{\partial \hat{D}_r}{\partial \zeta},$$
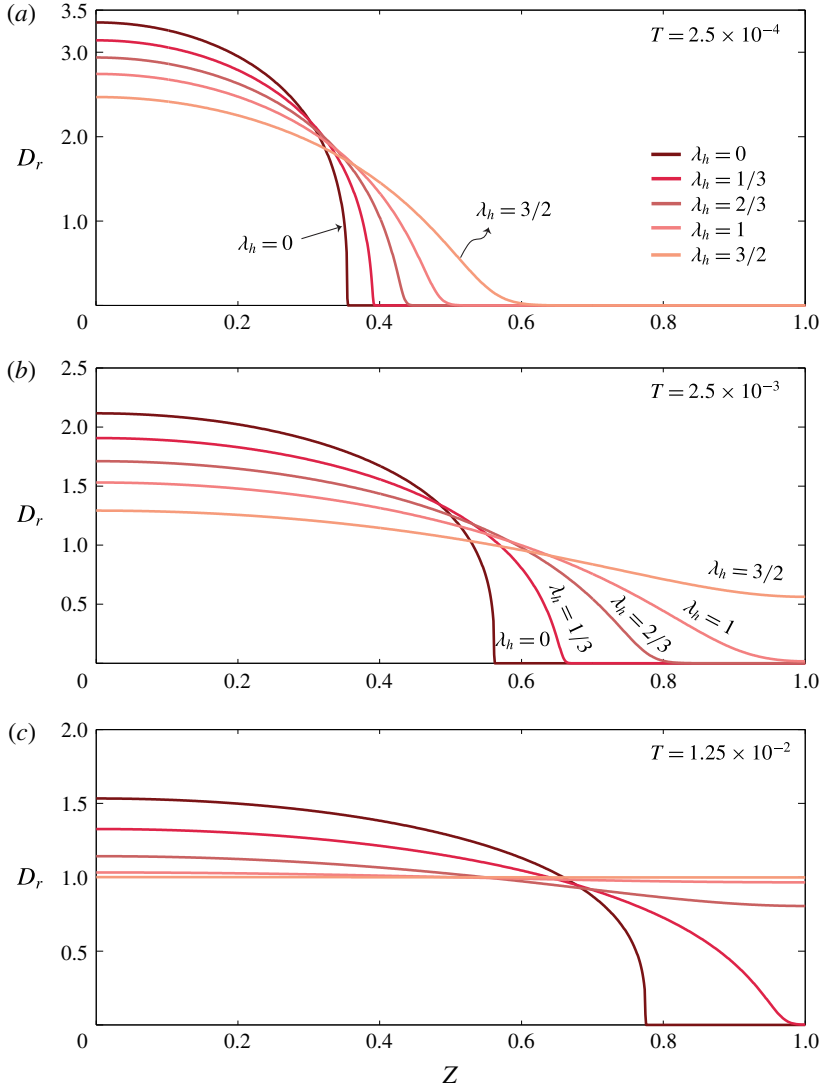
(4.16)

FIGURE 4. (Colour online) Source-type propagation over a prewetting layer in the tensile–viscous regime. Numerical solution corresponding to $0 \leqslant \lambda_h \leqslant 3/2$, $U_0 = 0$, $0 \leqslant T \leqslant 1/80$. Radial deformation plotted versus axial coordinate. Boundary conditions of type (4.15). $\lambda_h = 0$, $1/3$, $2/3$, 1, $3/2$ from dark to light reds respectively. (a) Solution at time $T = 1/4000$, (b) solution at time $T = 1/400$, (c) solution at time $T = 1/80$.

where we have denoted the time derivative of the front location Z_F by $\dot{Z}_F$. The contributions of the terms of (4.16) are on the left-hand side: bending and tension forces, and on the right-hand side: viscous pressure drop and shear forces.

4.2.1. *The bending–tension regime* $\lambda_h \gg (\epsilon \sqrt{\varepsilon_2})^{1/3}$

When $\lambda_h \gg (\epsilon \sqrt{\varepsilon_2})^{1/3}$ a dominant balance is achieved between the bending and tension terms of (4.16) on the length scale of $\delta \sim \epsilon \sqrt{\varepsilon_2} = \sqrt{r_b w}/l$. In the prewetting thickness range $(\epsilon \sqrt{\varepsilon_2})^{1/3} \ll \lambda_h \ll 1$ a uniform approximation matching the interior

profile (4.9) to the boundary layer solution can be attained in closed form. To this end we define $\hat{D}_r = T^{-1/5}\hat{D}_{r,1}$ and $\delta = \epsilon\sqrt{\varepsilon_2}Z_F^{-1}/[12(1-\nu^2)]^{1/4}$. Equation (4.16) reduces to,

$$\frac{\mathrm{d}^4\hat{D}_{r,1}}{\mathrm{d}\zeta^4} + \hat{D}_{r,1} \sim \beta \int_0^\zeta \hat{D}_{r,1}, \tag{4.17}$$

where $\beta = \delta Z_F \dot{Z}_F / 4\lambda_h^3 \ll 1$. The right-hand side of (4.17) must be retained in order to meet the boundary conditions at the front. These will be assumed as follows: $P = \hat{D}_{r,1} = \mathrm{d}\hat{D}_{r,1}/\mathrm{d}\zeta = 0$ at $\zeta = 0$. For large ζ, $\hat{D}_{r,1}$ must be bounded and satisfy the matching condition,

$$\lim_{\zeta \to \infty} \hat{D}_{r,1}(\zeta) = \lim_{\xi \to 1} \eta_F^{2/3}F(\xi), \tag{4.18}$$

where F and η_F correspond to the self-similar profile of (4.9) defined in (4.3). The asymptotic solution of (4.17) reads,

$$\hat{D}_{r,1} \sim (2\delta)^{1/3}\mathrm{e}^{\beta\zeta} - (2\delta)^{1/3}\exp\left[-\left(\frac{1}{\sqrt{2}} + \frac{\beta}{4}\right)\zeta\right]$$
$$\times \left[(1 + \sqrt{2}\beta)\sin\left(\frac{\zeta}{\sqrt{2}}\right) + \cos\left(\frac{\zeta}{\sqrt{2}}\right)\right]. \tag{4.19}$$

We cannot match the boundary layer and interior profiles in a straightforward manner due to the difference in functional form. In order to pursue a matched uniform solution we define the auxiliary problem,

$$\frac{\mathrm{d}^4\hat{D}_{r,1}^a}{\mathrm{d}\zeta^4} + \hat{D}_{r,1}^a \sim (2\delta)^{1/3}\zeta^{1/3}, \tag{4.20}$$

which differs from (4.17) by the small orders $O(\beta, \delta^{1/3})$. The solution of (4.20) reads,

$$\hat{D}_{r,1}^a = \hat{F}_p(\zeta) - \mathrm{e}^{-\zeta/\sqrt{2}}\left[\left(\hat{F}_p(0) + \sqrt{2}\frac{\mathrm{d}\hat{F}_p(0)}{\mathrm{d}\zeta}\right)\sin\frac{\zeta}{\sqrt{2}} + \hat{F}_p(0)\cos\frac{\zeta}{\sqrt{2}}\right], \tag{4.21}$$

and the particular solution $\hat{F}_p$ is given in appendix B. The auxiliary variable $\hat{D}_{r,1}^a$ satisfies (4.18) exactly and can be matched in closed form to the interior profile. A leading-order uniform approximation D_r^u can be written in the original variables,

$$D_r^u(Z, T) = T^{-1/5}\left[\left(1 - \frac{L_1^2}{4}\right)_+^{1/3} - (2 - L_1)_+^{1/3}\right] + T^{-1/5}\hat{F}_p(KL_2)$$
$$- T^{-1/5}\exp\left(-\frac{KL_2}{\sqrt{2}}\right)\left[(\hat{F}_p(0) + \sqrt{2}\hat{F}_p'(0))\sin\left(\frac{KL_2}{\sqrt{2}}\right) + \hat{F}_p(0)\cos\left(\frac{KL_2}{\sqrt{2}}\right)\right], \tag{4.22}$$

where $L_1 = \sqrt{3/10}ZT^{-1/5}$, $L_2 = \sqrt{40/3}T^{1/5} - Z$ and $K = [12(1-\nu^2)]^{1/4}/(\epsilon\sqrt{\varepsilon_2})$. The solution is plotted in figure 5 at $T = T_b(\alpha = 1/5)$, where transition from a tension dominant to a bending–tension regime is illustrated for two axial length scales $\delta = 0.005, 0.01$ (wall thickness and aspect ratios are adjusted accordingly).
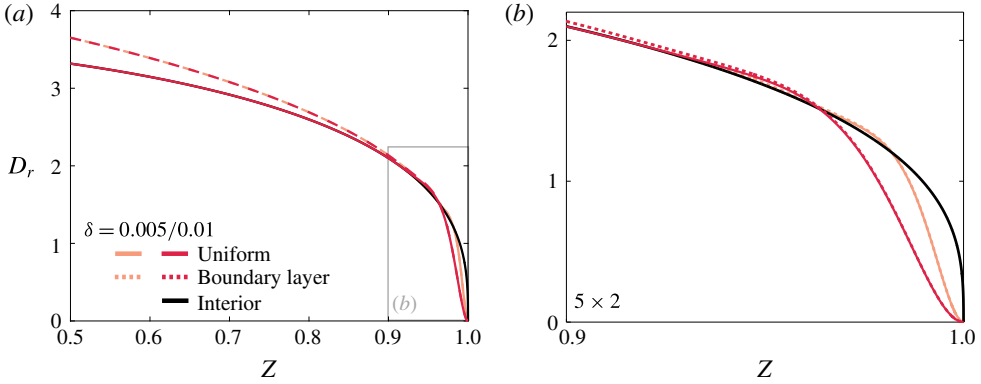
FIGURE 5. (Colour online) Uniform closed-form solution of a propagating elastohydrodynamic front for impulse-type boundary condition (4.8) and $\delta^{1/3} \ll \lambda_h \ll 1$. Snapshot of $D_r^u(Z, T_b)$ for $\delta = 0.01$ (red), $\delta = 0.005$ (coral) and corresponding boundary layer solutions (4.21) (dashed lines). The interior profile $\eta_F^{5/3} F(Z)$ (4.9) is plotted in black.
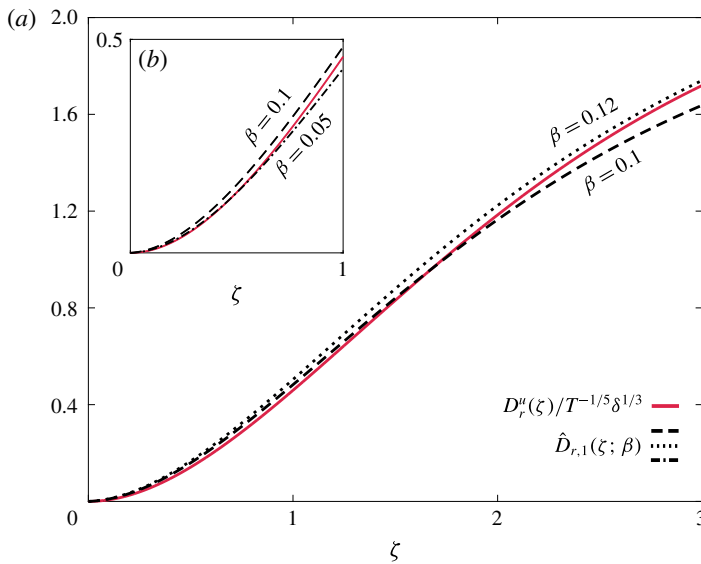

FIGURE 6. (Colour online) Convergence of the uniform solution (4.22) to the unmatched boundary layer solution (4.19) near the contact line. (*a*) The self-similar profile $D_r^u(\zeta)/T^{-1/5}\delta^{1/3}$ (solid red) is plotted against the boundary layer coordinate ζ for $\beta = 0.1$ (dashed), $\beta = 0.12$ (dotted). (*b*) Magnification of the region $0 \leqslant \zeta \leqslant 1$, $D_r^u(\zeta)/T^{-1/5}\delta^{1/3}$ (solid red) versus ζ for $\beta = 0.1$ (dashed), $\beta = 0.05$ (dashed-dotted).

The uniform solution converges to the ZKB profile (4.9) as $T \to \infty$. The convergence of the uniform solution (4.22) to the exact unmatched boundary layer solution (4.19) near the contact line is shown in figure 6 for various values of β.

At larger prewetting scales the effect of the boundary layer adjustment will diminish but will still impose shape modifications near the edge, due to the change in regime. A numerical solution and matching of the interior (e.g. (4.14)) and boundary layer (4.17)

regions is required to describe this behaviour. A similar problem was addressed in the late time spreading of an elastic plated gravity current (Hewitt *et al.* 2015).

4.2.2. *Smaller scales of the prewetting thickness* $\lambda_h \ll (\epsilon \sqrt{\varepsilon_2})^{1/3}$

We return to the dominant balance of equation (4.16). When $\varepsilon_1^5 \varepsilon_2 / \epsilon^3 \ll \lambda_h \ll (\epsilon \sqrt{\varepsilon_2})^{1/3}$ bending forces will balance viscous forces on the length scale of $\delta \sim (\epsilon^4 \varepsilon_2^2 \lambda_h^3)^{1/5}$ while shear forces remain negligible. This regime describes the early stages of fluid injection at the inlet, for which $Z_F \ll \sqrt{r_b w}/l$, and is analogous to the early time spreading of an elastic Hele-Shaw cell (Lister *et al.* 2013) or the pure bending regime of an elastic plated gravity current as described by Hewitt *et al.* (2015). We note that the assumptions on the boundary conditions near the contact line (solution of (4.17)) no longer hold at smaller prewetting thicknesses as discussed herein.

When $\lambda_h \ll \varepsilon_1^5 \varepsilon_2 / \epsilon^3$ bending forces will balance shear forces while viscous forces become negligible relative to these. However, the resulting axial length scale $\delta \sim \epsilon (\varepsilon_2 \lambda_h^2 / \varepsilon_1)^{1/3}$ is comparable with the shell thickness and hence we have reached the limit of the thin shell elastic model used in the analysis.

4.3. *Designing deformation patterns with application to soft actuators*

In this section we illustrate the use of the transport term $U_0 \cdot \partial D_r / \partial Z$ of (3.34*b*) and the relation between the speed of displacement propagation and the gap (λ_h), in order to obtain isolated moving deformations. The linear transport term may represent a relative motion of the rigid cylinder, or alternatively, $U_0(T)$ can be thought of as a slip velocity condition induced by an electric zeta potential or a similar mechanism.

The transported ZKB profile can be used as a building block for creating complex deformation patterns. Such mechanism may be useful for micro-swimmers (replacing complex mechanisms such as in Setter *et al.* 2012), as well as for soft-actuator and soft-robotic applications. Current soft robots commonly use multiple pressure inlets to compress various internal cavities and deform different parts of the robot (Tolley *et al.* 2014; Marchese & Rus 2015). In a previous work (Elbaz & Gat 2014) we suggested applying a viscous fluid to increase the possible modes of deformation for a given channel geometry. In this section we suggest a soft actuator with an initially closed embedded cavity, where viscous peeling dynamics advancing into the channel will limit the deformation to the region behind the peeling front, thus isolating the deformed region. Furthermore, applying the transport term in combination with the inlet pressure enables the design of moving isolated deformation patterns, thus allowing to temporally activate and deactivate different regions of the actuator.

We incorporate a small prewetting layer $\lambda_h \ll 1$, and focus on the tensile–viscous regime, neglecting boundary layer regularization for the moment. Equation (3.34*b*) is then simply,

$$\frac{\partial D_r}{\partial T} + 24 U_0 \frac{\partial D_r}{\partial Z} \sim 4 \frac{\partial}{\partial Z} \left\{ \frac{\partial D_r}{\partial Z} (\lambda_h + D_r)^3 \right\}. \qquad (4.23)$$

At the left boundary we employ an impulse sequence of the form,

$$D_r(0, T) = \sum_{n=0}^{N} A_n \left[\Theta \left(T + \frac{\Delta T_n}{2} - \tau_n \right) - \Theta \left(T - \frac{\Delta T_n}{2} - \tau_n \right) \right], \qquad (4.24)$$

where Θ is the Heaviside function. The signal is modulated in amplitude, A_n, and in width ΔT_n and can be sequenced non-uniformly by τ_n. We set a zero initial condition and a no-flux condition at the right boundary,

$$D_r(Z, 0) = 0, \quad \frac{\partial D_r(1, T)}{\partial Z} = 0. \tag{4.25a,b}$$

Under the above conditions, a sequence of symmetric ZKB profiles will propagate through the interface. Assuming sufficiently small λ_h, each pulse will propagate independently. The rate of diffusion of the profiles decays strongly beneath a certain amplitude (determined by (3.35)) and is significantly slower than the rate of their transport, that is, they maintain their forms as they are transported. Using this approach, isolated fluid segments can be generated arbitrarily and transported along the interface independent of the pressure gradient and having limited or negligible communication with each other. In particular, the boundary sequence (4.24) can be modulated to form a moving wave signal, as illustrated in figure 7 via numerical solution of (4.23)–(4.25). A prewetting layer of $\lambda_h = 0.15$ was used with a constant rigid cylinder motion of $U_0 = 2$. Figure 7(b) shows 3 progressive snapshots of the resulting radial deformation wave as it propagates the interface. The corresponding contour plot is given in figure 7(a) and shows the uniformity of the sequence beyond an early generation time, $T > 7 \times 10^{-3}$. The obtained solution closely approximates the waveform,

$$D_r(Z, T) \approx \frac{A}{2}[1 + \sin(KZ - \Omega T)], \quad \frac{\Omega}{K} = \frac{U_0}{2}, \tag{4.26a,b}$$

where $A = 0.1$ and $K = \Omega = 10\pi$.

5. Concluding remarks

The analysis presented here assumes several small parameters, including geometric requirements such as $\varepsilon_2 = w/r_i \ll 1$ and dynamic physical requirements such as small deformations $\varepsilon_3 = d_r^*/r_b \ll 1$ and negligible inertia $\varepsilon_1 Re = \rho \epsilon^2 r_b^2 p^{*5}/\mu^2 (E\varepsilon_2)^4 \ll 1$. While the geometric requirements are given and constant for a specific configuration, the physical requirements depend on, and limit, the magnitude of the characteristic driving pressure. To illustrate the maximal allowable pressures and characteristic time scales we examine several configurations with constant geometric ratios $\epsilon = \varepsilon_2 = 0.1$. For water ($\mu = 10^{-3}$ (Pa s), $\rho = 10^3$ (Kg m^{-3})) as the liquid and rubber ($E = 10^9$ (Pa)) as the tube, we obtain $p^* = 10^4$ (Pa), $t^* = 10^4$ (s) in the case of $r_b = 1$ (m) and $p^* = 6.3 \times 10^4$ (Pa), $t^* = 4$ (s) in the case of $r_b = 10^{-2}$ (m). For silicon oil ($\mu = 10$ (Pa s), $\rho = 7.5 \times 10^2$ (Kg m^{-3})) and rubber ($E = 10^9$ (Pa)), we obtain $p^* = 4.2 \times 10^5$ (Pa), $t^* = 10^2$ (s) in the case of $r_b = 1$ (m) and $p^* = 2.6 \times 10^6$ (Pa), $t^* = 0.5$ (s) in the case of $r_b = 10^{-2}$ (m). Hence, a wide range of characteristic driving pressures and time scales can be achieved by varying the properties of the configuration. Unlike the linear elastohydrodynamics examined in Elbaz & Gat (2014), the assumption of creeping flow in the current problem can be achieved for any configuration, as long as p^* and λ_h are sufficiently small.

Future research may include the effect of varying tube wall thickness, which is similar to spatially varying surface tension, and may allow for transport of isolated deformations without external mechanisms such as presented in § 4.3.
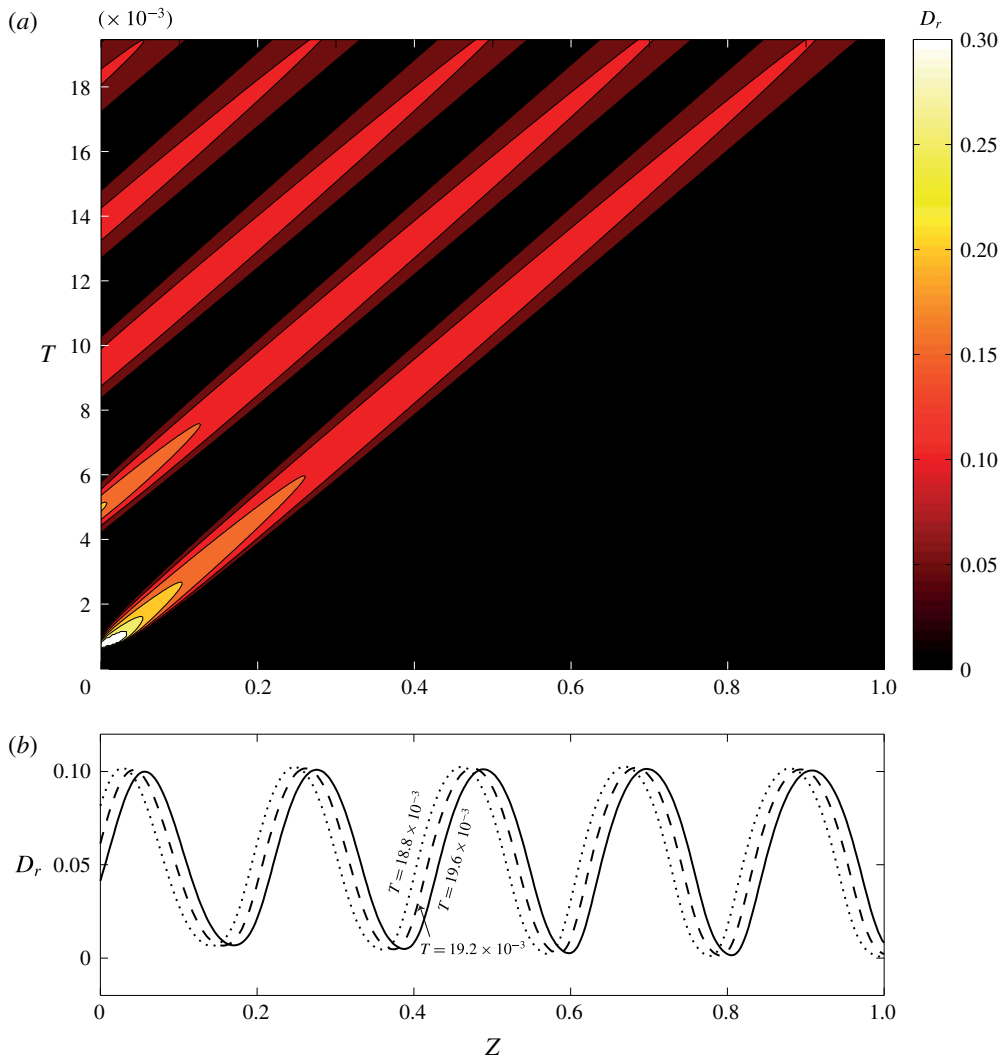
FIGURE 7. (Colour online) Moving wave deformation pattern generated via a modulated impulse sequence (4.24). A prewetting layer of $\lambda_h = 0.15$ is used upon constant rigid cylinder motion of $U_0 = 2$. Modulation laws in the interval $0 \leqslant T \leqslant 0.02$: $A_n = [0.37, 0.54, 0.54, 0.54, 0.54]$, $\tau_n = [0.8, 5.0, 9.3, 13.8, 18.3] \times 10^{-3}$, $\Delta T_n = [0.125, 0.65, 0.9, 1.1, 1.25] \times 10^{-3}$, $n = 1 \ldots 5$. (*a*) Fluid pressure contour in space and time. (*b*) Three progressive snapshots of the radial deformation wave at times $T = [18.8, 19.2, 19.6] \times 10^{-3}$, as it propagates the interface.

Acknowledgement

Appendix A. Summary of results in dimensional form

Governing equations of the elastohydrodynamics in fluid pressure p and elastic radial deformation d_r, corresponding to (3.34),

$$\frac{Ew^3}{12(1-\nu^2)}\frac{\partial^4 d_r}{\partial z^4} - \frac{1}{2}\left[\frac{\mu w u_0}{(h_0 + d_r)^2} - \frac{w}{2}\frac{\partial p}{\partial z}\right]\frac{\partial d_r}{\partial z} + \frac{Ew}{r_b^2}d_r - \frac{w(h_0 + d_r)}{4}\frac{\partial^2 p}{\partial z^2} \sim p, \quad (A\,1a)$$

$$\frac{\partial d_r}{\partial t} - \frac{1}{12\mu}\frac{\partial}{\partial z}\left\{\frac{\partial p}{\partial z}(h_0 + d_r)^3\right\} + \frac{u_0}{2}\frac{\partial d_r}{\partial z} \sim 0. \quad (A\,1b)$$

Interior tensile–viscous regime solution of impulse driven propagation according to self-similarity, corresponding to (4.9),

$$d_r(z,t) = \frac{p^{*2/5}r_b^{6/5}(48\mu l^2)^{1/5}}{(Ew)^{3/5}}t^{-1/5}\left[1 - \frac{3}{40}\left(\frac{48(Ew)^2\mu}{p^{*3}l^3 r_b^4}\right)^{2/5}z^2 t^{-2/5}\right]_+^{1/3}, \quad (A\,2)$$

where $(s)_+ = \max(s, 0)$.

Self-similar propagation laws for inlet signals of type (4.5), corresponding to (4.10),

$$z_F(t, \alpha) = l\left(\frac{p^{*3}r_b^4 t}{48\mu l^2(Ew)^2}\right)^{(1-3\alpha)/2}\eta_F(\alpha), \quad (A\,3a)$$

$$v(t, \alpha) = 2\pi r_b^2 l(48)^{(5\alpha-1)/2}\left(\frac{Ew}{r_b}\right)^{5\alpha-2}p^{*(5-15\alpha)/2}\left(\frac{t}{\mu}\right)^{(1-5\alpha)/2}Q(\alpha), \quad (A\,3b)$$

$$t_b(\alpha) = \frac{48\mu l^2(Ew)^2}{p^{*3}r_b^4}\eta_F(\alpha)^{-2/(1-3\alpha)}. \quad (A\,3c)$$

Here, v is the interface volume.

Appendix B. Particular solution of (4.20)

$$\begin{aligned}
\hat{F}_p(\zeta) = \frac{\delta^{1/3}}{\sqrt{2}}\Bigg\{ &(-1+i)(-1-i)^{2/3}\exp\left(-\frac{\zeta}{\sqrt{2}}\right)\cos\left(\frac{\zeta}{\sqrt{2}}\right)\hat{\Gamma}\left(\frac{4}{3}, -\frac{(1+i)\zeta}{\sqrt{2}}\right)\\
&+ (-1-i)(-1+i)^{2/3}\exp\left(-\frac{\zeta}{\sqrt{2}}\right)\cos\left(\frac{\zeta}{\sqrt{2}}\right)\hat{\Gamma}\left(\frac{4}{3}, -\frac{(1-i)\zeta}{\sqrt{2}}\right)\\
&+ (1+i)(1-i)^{2/3}\exp\left(\frac{\zeta}{\sqrt{2}}\right)\cos\left(\frac{\zeta}{\sqrt{2}}\right)\hat{\Gamma}\left(\frac{4}{3}, \frac{(1-i)\zeta}{\sqrt{2}}\right)\\
&+ (1-i)(1+i)^{2/3}\exp\left(\frac{\zeta}{\sqrt{2}}\right)\cos\left(\frac{\zeta}{\sqrt{2}}\right)\hat{\Gamma}\left(\frac{4}{3}, \frac{(1+i)\zeta}{\sqrt{2}}\right)\\
&- (1+i)^{5/3}\exp\left(-\frac{\zeta}{\sqrt{2}}\right)\sin\left(\frac{\zeta}{\sqrt{2}}\right)\hat{\Gamma}\left(\frac{4}{3}, -\frac{(1+i)\zeta}{\sqrt{2}}\right)\\
&- (1-i)^{5/3}\exp\left(-\frac{\zeta}{\sqrt{2}}\right)\sin\left(\frac{\zeta}{\sqrt{2}}\right)\hat{\Gamma}\left(\frac{4}{3}, -\frac{(1-i)\zeta}{\sqrt{2}}\right)\\
&+ (1-i)^{5/3}\exp\left(\frac{\zeta}{\sqrt{2}}\right)\sin\left(\frac{\zeta}{\sqrt{2}}\right)\hat{\Gamma}\left(\frac{4}{3}, \frac{(1-i)\zeta}{\sqrt{2}}\right)\\
&+ (1+i)^{5/3}\exp\left(\frac{\zeta}{\sqrt{2}}\right)\sin\left(\frac{\zeta}{\sqrt{2}}\right)\hat{\Gamma}\left(\frac{4}{3}, \frac{(1+i)\zeta}{\sqrt{2}}\right)\Bigg\} \quad (B\,1)
\end{aligned}$$

where $\delta = \epsilon\sqrt{\varepsilon_2}\sqrt{3/40}T^{-1/5}/[12(1-\nu^2)]^{1/4}$ and $\hat{\Gamma}$ is the upper incomplete gamma function.

REFERENCES

AL-HOUSSEINY, T. T., CHRISTOV, I. C. & STONE, H. A. 2013 Two-phase fluid displacement and interfacial instabilities under elastic membranes. *Phys. Rev. Lett.* **111** (3), 034502.

BALMFORTH, N. J., CRASTER, R. V. & HEWITT, I. J. 2015 The speed of an inclined ruck. *Proc. R. Soc. Lond.* A **471**, 20140740.

BARENBLATT, G. I. 1952 On some unsteady fluid and gas motions in a porous medium. *Prikl. Mat. Mekh.* **16** (1), 67–78; in Russian.

BUCKMASTER, J. 1977 Viscous sheets advancing over dry beds. *J. Fluid Mech.* **81** (04), 735–756.

CARLSON, A., MANDRE, S. & MAHADEVAN, L. 2015 Elastohydrodynamics of contact in adherent sheets. arXiv:1508.06234.

CHAUHAN, A. & RADKE, C. J. 2002 Settling and deformation of a thin elastic shell on a thin fluid layer lying on a solid surface. *J. Colloid Interface Sci.* **245** (1), 187–197.

DUGDALE, D. S. & RUIZ, C. 1971 *Elasticity for Engineers*. McGraw-Hill.

ELBAZ, S. B. & GAT, A. D. 2014 Dynamics of viscous liquid within a closed elastic cylinder subject to external forces with application to soft robotics. *J. Fluid Mech.* **758**, 221–237.

GAD-EL HAK, M. 2002 Compliant coatings for drag reduction. *Prog. Aerosp. Sci.* **38** (1), 77–99.

HALPERN, D. & GROTBERG, J. B. 1992 Fluid-elastic instabilities of liquid-lined flexible tubes. *J. Fluid Mech.* **244**, 615–632.

HEWITT, I. J., BALMFORTH, N. J. & DE BRUYN, J. R. 2015 Elastic-plated gravity currents. *Eur. J. Appl. Maths* **26** (01), 1–31.

HOSOI, A. E. & MAHADEVAN, L. 2004 Peeling, healing, and bursting in a lubricated elastic sheet. *Phys. Rev. Lett.* **93** (13), 137802.

HOWELL, P. D., ROBINSON, J. & STONE, H. A. 2013 Gravity-driven thin-film flow on a flexible substrate. *J. Fluid Mech.* **732**, 190–213.

HUPPERT, H. E. 1982 The propagation of two-dimensional and axisymmetric viscous gravity currents over a rigid horizontal surface. *J. Fluid Mech.* **121**, 43–58.

LISTER, J. R. & KERR, R. C. 1989 The propagation of two-dimensional and axisymmetric viscous gravity currents at a fluid interface. *J. Fluid Mech.* **203**, 215–249.

LISTER, J. R., PENG, G. G. & NEUFELD, J. A. 2013 Viscous control of peeling an elastic sheet by bending and pulling. *Phys. Rev. Lett.* **111** (15), 154501.

LOVE, A. E. H. 1888 The small free vibrations and deformations of a thin elastic shell. *Phil. Trans. R. Soc. Lond.* A **179**, 491–546.

MARCHESE, A. D. & RUS, D. 2015 Design, kinematics, and control of a soft spatial fluidic elastomer manipulator. *Intl J. Robotics Res.* doi:10.1177/0278364915587925.

MCEWAN, A. D. & TAYLOR, G. I. 1966 The peeling of a flexible strip attached by a viscous adhesive. *J. Fluid Mech.* **26** (01), 1–15.

MOLLMANN, H. 1981 *Introduction to the Theory of Thin Shells*. Wiley.

MOMONIAT, E. 2006 Axisymmetric spreading of a thin drop under gravity and time-dependent non-uniform surface tension. *J. Math. Anal. Appl.* **322** (1), 41–50.

PAIDOUSSIS, M. P. 1998 *Fluid-Structure Interactions: Slender Structures and Axial Flow*, vol. 1. Academic.

PIHLER-PUZOVIĆ, D., ILLIEN, P., HEIL, M. & JUEL, A. 2012 Suppression of complex fingerlike patterns at the interface between air and a viscous fluid by elastic membranes. *Phys. Rev. Lett.* **108** (7), 074502.

PIHLER-PUZOVIĆ, D., JUEL, A. & HEIL, M. 2014 The interaction between viscous fingering and wrinkling in elastic-walled Hele-Shaw cells. *Phys. Fluids* **26** (2), 022102.

RUS, D. & TOLLEY, M. T. 2015 Design, fabrication and control of soft robots. *Nature* **521** (7553), 467–475.

SETTER, E., BUCHER, I. & HABER, S. 2012 Low-Reynolds-number swimmer utilizing surface traveling waves: analytical and experimental study. *Phys. Rev.* E **85** (6), 066304.

TOLLEY, M. T., SHEPHERD, R. F., MOSADEGH, B., GALLOWAY, K. C., WEHNER, M., KARPELSON, M., WOOD, R. J. & WHITESIDES, G. M. 2014 A resilient, untethered soft robot. *Soft Robot.* **1** (3), 213–223.

TOPPALADODDI, S. & BALMFORTH, N. J. 2014 Slender axisymmetric stokesian swimmers. *J. Fluid Mech.* **746**, 273–299.

TRINH, P. H., WILSON, S. K. & STONE, H. A. 2014a A pinned or free-floating rigid plate on a thin viscous film. *J. Fluid Mech.* **760**, 407–430.

TRINH, P. H., WILSON, S. K. & STONE, H. A. 2014b An elastic plate on a thin viscous film. arXiv:1410.8558.

WHITE, J. P. & HEIL, M. 2005 Three-dimensional instabilities of liquid-lined elastic tubes: a thin-film fluid-structure interaction model. *Phys. Fluids* **17** (3), 031506.

ZEL'DOVICH, Y. B. & KOMPANEETS, A. S. 1950 Towards a theory of heat conduction with thermal conductivity depending on the temperature. In *Collection of Papers Dedicated to 70th Anniversary of A. F. Ioffe*, vol. 1, pp. 61–72. Izvestiya Akademii Nauk SSSR.